Accelerated adiabatic passage in cavity magnomechanics

Shi-fan Qi and Jun Jing[*]

Department of Physics, Zhejiang University, Hangzhou 310027, Zhejiang, China

Cavity magnomechanics provides a readily controllable hybrid system, consisting of a cavity mode, magnon mode, and phonon mode, for quantum state manipulation and transfer. To implement a fast-and-robust state transfer between the hybrid photon-magnon mode and the phonon mode, we apply two accelerated-adiabatic-passage protocols based on the counterdiabatic Hamiltonian for transitionless quantum driving and the Levis-Riesenfeld invariant for inverse engineering. We construct the counterdiabatic Hamiltonian in a state-resolved way and express it through the creation and annihilation operators rather than the system eigenstates and their time derivatives. We can optimize the invariant-based inverse-engineering protocol with respect to the stability against the systematic errors of the coupling strength and frequency detuning. Both protocols apply for continuous-variable systems with arbitrary target states. We also discuss the decoherence effects from the thermal environment and the counterrotating interactions on both protocols. Our work contributes to the quantum memory for photonic and magnonic quantum information.

I. INTRODUCTION

Hybrid cavity-magnon systems [1–3] based on the expedient control of coherent magnon-photon coupling have recently attracted intensive attention. They have led to new avenues for quantum computing [4], quantum communication [5], and quantum sensing [6]. Analogous to cavity quantum electrodynamics (QED) [7] and optomechanics [8], cavity magnomechanics [9] developed rapidly as a mesoscopic platform for quantum information processing for both theoretical [10–13] and experimental [14–21] aspects. Active investigations of magnon-based quantum information transfer are focusing on the coupling between photons and magnons and that between magnons and phonons in ferrimagnetic materials. Typical applications of these couplings include hybrid entanglement and steering [22–25], the photon-phonon interface [26,27], and the magnomechanical phonon laser [28].

In particular, a cavity magnomechanical system [9] consists of a single-crystal yttrium iron garnet (YIG) sphere placed inside a microwave cavity, where the magnon modes formed by the excitations of the collective angular momentum of the spins in such a magnetic-material sphere are coupled with the deformation phonon modes via a magnetostrictive force and also with the electromagnetic cavity modes via a magnetic dipole interaction. The phonon in the YIG sphere decays at a rate of about 100 Hz [9,22], which is much smaller than its own frequency and those of the magnon and the photon. That enables the storage and transfer of the microwave photonic and magnonic states as long-lasting modes, constituting a key step for future quantum communication networks [29]. Inspired by the light-matter interface implemented in cavity QED [30,31], optomechanical systems [32–34], and

optical waveguides [35], stimulated Raman adiabatic passage between a photon and a phonon [27] and magnon-assisted photon-phonon conversion [26] have been proposed in cavity magnomechanical systems. The use of adiabatic evolution or elimination in these protocols, however, prolongs the exposure to errors of quantum-mechanical origin, leading to the environment-induced decoherence. This calls for a decrease in the run time of the adiabatic paths in cavity magnomechanical systems through shortcut-to-adiabatic (STA) protocols.

Various STA approaches [36,37], including the transitionless quantum driving (TQD) based on the counterdiabatic (CD) Hamiltonian [38–40] and the inverse-engineering methods by virtue of the Lewis-Riesenfeld (LR) invariant [41], the time rescaling [42], or the noise-induced adiabaticity [43–45], have been applied to several prototypes, such as two- and three-level atomic systems [46–48], quantum harmonic oscillators [49], optomechanical systems [50–52], and coupled-waveguide devices [35]. In contrast to the existing STA methods, which are limited to discrete systems or continuous-variable systems in a subspace of a fixed number of excitations [51–53], our protocol in this work is independent of the target state and adapts to any coupled harmonic oscillators. In addition, the stability of our STA protocol in the cavity magnomechanical system for state transfer can be optimized with respect to its robustness against the systematic errors [53–56] that result mainly from the intensity fluctuation or inaccurate realization of the time-dependent driving laser.

The rest of this work is structured as follows. In Sec. II, we introduce a hybrid quantum model for cavity magnomechanics and then provide an effective Hamiltonian describing the interaction between the hybrid photon-magnon mode and the phonon mode. The details of the derivation can be found in the Appendix. Based on the effective Hamiltonian, we propose two STA protocols in Sec. III for a fast-and-faithful state transfer in cavity magnomechanical systems.
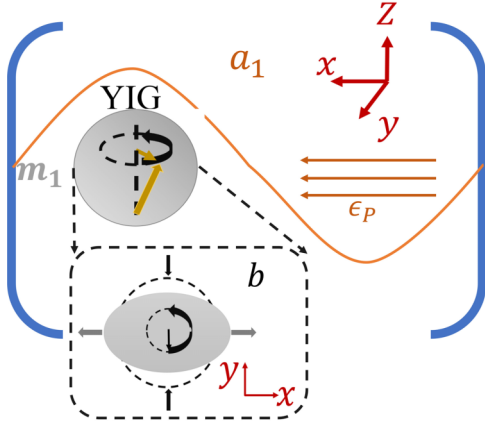
*jingjun@zju.edu.cn

FIG. 1. Schematic diagram of a YIG sphere placed in a microwave cavity near the maximum magnetic field of the cavity mode. The uniform bias magnetic field exciting the Kittel mode in the YIG and establishing the magnon-photon coupling is aligned along the z axis. The photon mode is driven by a microwave source along the x axis (with a Rabi frequency ϵ_p). The inset shows how the dynamic magnetization of a magnon (vertical black arrows) causes the deformation (compression along the y direction) of the YIG sphere (and vice versa), which rotates at the magnon frequency.

In Sec. III A, we provide a transparent construction of the counterdiabatic Hamiltonian for TQD, which can be rigorously expressed by the creation and annihilation operators of the bosonic modes. In Sec. III B, we derive a general Levis-Riesenfeld invariant for a two-coupled-bosonic-mode system, which also applies to arbitrary target states. Under a general formalism for the systematic error of the effective Hamiltonian, the error sensitivities of the π-pulse protocol, TQD, and invariant-based STA are analyzed and optimized in Secs. IV A, IV B, and IV C, respectively. In Sec. V, we discuss the effects of thermal noise and counterrotating interaction on the transport protocols using the master equation and numerical simulation, respectively. This work is summarized in Sec. VI.

II. MODEL

Consider a hybrid system in the cavity-magnonic setup shown in Fig. 1, where a YIG sphere is inserted into a microwave cavity. The system is constituted by the microwave-mode photons, the magnons, and the mechanical-mode phonons, which has been experimentally realized in the dispersive regime [9]. The magnons are coupled to photons via the Zeeman interaction and to phonons by the magnetization interaction. The temporally varying magnetization induced by the magnon excitation inside the YIG sphere leads to the deformation of its geometrical structure, which forms the vibrational modes (phonons) of the sphere. The Hamiltonian of the full system is given by ($\hbar \equiv 1$)

$$H_0 = \omega_a a_1^\dagger a_1 + \omega_m m_1^\dagger m_1 + \omega_b b^\dagger b + g_{mb} m_1^\dagger m_1 (b + b^\dagger)$$
$$+ g_{ma}(a_1 m_1^\dagger + a_1^\dagger m_1) + i(\epsilon_p a_1^\dagger e^{-i\omega_p t} - \epsilon_p^* a_1 e^{i\omega_p t}), \quad (1)$$

where a_1 ($a_1^\dagger$), m_1 ($m_1^\dagger$), and b ($b^\dagger$) are the annihilation (creation) operators of the microwave cavity mode, the magnon

of the ground Kittel mode, and the mechanical mode with transition frequencies ω_a, ω_m, and ω_b, respectively. The magnon-mode frequency is $\omega_m = \gamma h$, where γ is the gyromagnetic ratio and h is the external bias magnetic field. Thus, the frequency ω_m can be temporally tuned by the external magnetic field. g_{ma} and g_{mb} are, respectively, the single-excitation coupling strengths of the photon-magnon interaction and magnon-phonon interaction. The last term in H_0 describes the external driving of the photon mode, where ω_p is the driving frequency and ϵ_p is the Rabi frequency of the driving field.

Following the standard linearization approach [8] and under the proper driving conditions, we can extract an effective Hamiltonian describing the interaction between a hybridized photon-magnon mode and the phonon mode (the details can be found in the Appendix):

$$H = (\Delta - \omega_b)m^\dagger m + (gm^\dagger b + g^* m b^\dagger). \quad (2)$$

Here $m = \sin\phi a_1 - \cos\phi m_1$ is the hybridized normal mode with $\tan(2\phi) \equiv 2g_{ma}/(\omega_a - \omega_m)$. g is the driving-enhanced coupling strength between the hybrid mode m and the mechanical mode b,

$$g = g_{mb} m_s \cos^2\phi - g_{mb} a_s \sin\phi\cos\phi, \quad (3)$$

where

$$m_s = \frac{\epsilon_p \sin\phi}{i\Delta + \kappa_m}, \qquad a_s = \frac{\epsilon_p \cos\phi}{i\Delta' + \kappa_a}, \quad (4)$$

with the effective frequencies of the hybridized modes

$$\Delta = \frac{\omega_a + \omega_m}{2} - \omega_p - \sqrt{\left(\frac{\omega_a - \omega_m}{2}\right)^2 + g_{ma}^2},$$
$$\Delta' = \frac{\omega_a + \omega_m}{2} - \omega_p + \sqrt{\left(\frac{\omega_a - \omega_m}{2}\right)^2 + g_{ma}^2} \quad (5)$$

and the decay rates κ_m and κ_a.

It is important to emphasize that the hybrid-mode frequency Δ and the coupling strength g can be modulated in timely fashion by the external magnetic bias field $h(t)$ [22] and the Rabi frequency of the driving field $\epsilon_p(t)$ [48]. The effective Hamiltonian in Eq. (2) can then be adapted to shortcut-to-adiabatic methods for state manipulation. Formally, the state transfer between the hybrid mode and the mechanical mode could be started from the time-dependent Hamiltonian

$$H(t) = \Delta(t)m^\dagger m + g(t)m^\dagger b + g^*(t)b^\dagger m, \quad (6)$$

where $\Delta(t) \equiv \Delta - \omega_b$. In the framework of the following protocols for rapid-and-faithful state transfer, it is instructive to transform the system Hamiltonian $H(t)$ into the rotating frame with respect to $U(t) = \exp[i\int_0^t ds\Delta(s)/2(m^\dagger m - b^\dagger b)]$,

$$H(t) = \frac{\Delta(t)}{2}(m^\dagger m - b^\dagger b) + g(t)m^\dagger b + g^*(t)b^\dagger m. \quad (7)$$

III. THE STATE-TRANSFER PROTOCOLS

A straightforward method to achieve the state transfer is to use a π pulse. In this case, one can require the driving frequency to be resonant with the hybrid mode m, i.e., $\Delta(t) = 0$ for all times in Hamiltonian (7). Then an initial state

$|\psi(0)\rangle = (\sum_k C_k|k\rangle_m)|0\rangle_b$ with arbitrary normalized coefficients C_k could be converted to

$$|\psi(T)\rangle = |0\rangle_m \left(\sum_k C_k e^{-i\frac{k\pi}{2}}|k\rangle_b \right) \qquad (8)$$

after a desired period T as long as the coupling strength satisfies $\int_0^T dt|g(t)| = \pi/2$. For example, for a flat π pulse one can set $g(t) = \pi/(2T)$. Note the final state for the mechanical mode b in $|\psi(T)\rangle$ is not exactly the same as the one for the hybrid mode m in the initial state $|\psi(0)\rangle$ regarding the dynamical phase $k\pi/2$. However, the phase difference between the final and initial states could be compensated with the local dynamical phase $e^{-ik\omega_b\tau}$ by $H_b = \omega_b b^\dagger b$ after a free evolution time τ, which satisfies $\omega_b\tau = 2n\pi - \pi/2$ with integer n. We therefore do not distinguish the states $\sum_k C_k e^{-ik\pi/2}|k\rangle$ and $\sum_k C_k|k\rangle$ when calculating the state-transfer fidelity. The state-transfer fidelity or efficiency is thus measured by the target-state population

$$P(t) = \sum_{C_k\neq 0} |\langle 0k|\psi(t)\rangle|^2, \qquad (9)$$

where $|\psi(t)\rangle$ is the dynamical state determined by the initial state $|\psi(0)\rangle$ and the effective Hamiltonian (7). Note that when the target state is a Fock state $|N\rangle$, P becomes the conventional fidelity.

The π-pulse protocol is straightforward but sensitive to the systematic errors [54], which are caused by the fluctuations of the Hamiltonian. The state transfer can also be achieved in an adiabatic way, which is robust to the systematic errors, but is prone to decoherence due to its long evolution time. The state-transfer protocol can be improved by accelerated adiabatic passages or shortcuts to adiabaticity that are believed to be robust against both decoherence and systematic errors. In the next two sections, we construct two STA protocols for TQD and the LR invariant for our hybrid magnomechanical model. Our results are presented with the state-transfer fidelity for the number state (Fock state) and the cat state as a superposition of both the coherent state and Fock state.

A. Transitionless quantum driving for continuous-variable system

The TQD approach depending on full knowledge of the instantaneous eigenstructure of the original Hamiltonian was proposed in the first decade of this century. Conventionally, if the original time-dependent Hamiltonian $H(t)$ could be formally expressed in the spectral representation as $H(t) = \sum_n E_n(t)|n(t)\rangle\langle n(t)|$, then assisted by an ancillary Hamiltonian, called the counterdiabatic Hamiltonian [36,38],

$$H_{CD}(t) = i\sum_n [1 - |n(t)\rangle\langle n(t)|]|\dot n(t)\rangle\langle n(t)|, \qquad (10)$$

the system could keep track of the instantaneous eigenstates of $H(t)$ at a much faster speed. This approach is also believed to be highly robust against control-parameter variations [36]. One can understand that it usually applies to the discrete systems, and it is explicitly represented by the eigenstates and their time derivatives.

In this section, we obtain the CD term expressed by the operators for the continuous-variable systems. With the unitary transformation [57], the Hamiltonian in Eq. (7) is diagonalized to be

$$H(t) = \omega_A A^\dagger A + \omega_B B^\dagger B, \qquad (11)$$

where $\omega_{A,B} = \pm\sqrt{\Delta^2 + 4g^2}/2$ and

$$\begin{aligned} A &\equiv \cos\theta m + \sin\theta b, \\ B &\equiv \sin\theta m - \cos\theta b, \end{aligned} \qquad (12)$$

with $\tan(2\theta) = 2g(t)/\Delta(t)$. To simplify the formation of the TQD protocol, the coupling strength $g(t)$ in this protocol is set to be real, i.e., $g(t) = g^*(t)$.

In the subspace with a fixed and arbitrary excitation number N, the CD Hamiltonian for the system Hamiltonian in Eq. (11) can be written as $H_{CD} = i\sum_{n=0}^N |\dot\epsilon_n\rangle\langle\epsilon_n|$, where the orthonormal eigenstates read

$$|\epsilon_{N-n}\rangle = \frac{1}{\sqrt{(N-n)!n!}}(A^\dagger)^{N-n}(B^\dagger)^n|0\rangle, \qquad (13)$$

with $|0\rangle$ being the vacuum state for both modes. Due to the fact that

$$\begin{aligned} \dot A &= -\dot\theta\sin\theta m + \dot\theta\cos\theta b = -\dot\theta B, \\ \dot B &= \dot\theta\cos\theta m + \dot\theta\sin\theta b = \dot\theta A, \end{aligned} \qquad (14)$$

we have

$$\begin{aligned} |\dot\epsilon_{N-n}\rangle &= -\dot\theta\sqrt{(n+1)(N-n)}|\epsilon_{N-n-1}\rangle \\ &\quad + \dot\theta\sqrt{n(N-n+1)}|\epsilon_{N-n+1}\rangle. \end{aligned} \qquad (15)$$

Then the CD Hamiltonian in Eq. (10) becomes

$$\begin{aligned} H_{CD} &= i\sum_{n=0}^N |\dot\epsilon_n\rangle\langle\epsilon_n| \\ &= -i\dot\theta\sum_{n=0}^{N-1}\sqrt{(N-n)(n+1)}|\epsilon_{N-n-1}\rangle\langle\epsilon_{N-n}| \qquad (16) \\ &\quad + i\dot\theta\sum_{n=1}^N \sqrt{n(N-n+1)}|\epsilon_{N-n+1}\rangle\langle\epsilon_{N-n}|. \end{aligned}$$

According to the definition in Eq. (13), the first term in Eq. (16) expands as

$$\begin{aligned} &\sum_{n=0}^{N-1}\sqrt{(N-n)(n+1)}|\epsilon_{N-n-1}\rangle\langle\epsilon_{N-n}| \\ &= \sum_{n=0}^{N-1}\sqrt{(N-n)(n+1)} \\ &\quad \times \frac{(A^\dagger)^{N-n-1}(B^\dagger)^{n+1}|0\rangle\langle 0|A^{N-n}B^n}{\sqrt{(N-n-1)!(n+1)!}\sqrt{(N-n)!n!}} \\ &= B^\dagger \sum_{n=0}^{N-1}\frac{(A^\dagger)^{N-n-1}(B^\dagger)^n|0\rangle\langle 0|A^{N-n-1}B^n}{(N-n-1)!n!}A \\ &= B^\dagger I_{N-1}A, \qquad (17) \end{aligned}$$

where I_{N-1} is the identity operator in the subspace with $N-1$ excitations. Similarly, the second term in Eq. (16) turns out to be

$$\sum_{n=1}^{N} \sqrt{n(N-n+1)} |\epsilon_{N-n+1}\rangle\langle\epsilon_{N-n}| = A^\dagger I_{N-1} B. \quad (18)$$

Note that N is arbitrary; then across subspaces with various excitation numbers, the CD Hamiltonian can be expressed as

$$H_{\rm CD} = i\dot\theta(A^\dagger B - B^\dagger A) = i\dot\theta(b^\dagger m - m^\dagger b). \quad (19)$$

Regarding the original Hamiltonian (7), the total Hamiltonian for the transitionless quantum driving reads

$$
\begin{aligned}
H_{\rm tot} &= H(t) + H_{\rm CD} \\
&= \frac{\Delta(t)}{2}(m^\dagger m - b^\dagger b) + [g(t) - i\dot\theta] m^\dagger b \\
&\quad + [g(t) + i\dot\theta] m b^\dagger,
\end{aligned} \quad (20)
$$

where the time dependence and the boundary conditions of the control parameter $\dot\theta$,

$$\dot\theta = \frac{\dot g \Delta - \dot\Delta g}{\Delta^2 + 4g^2}, \quad (21)$$

determine the pattern and the speed of the accelerated adiabatic passage. The system Hamiltonian in Eq. (7) can be rewritten in the form

$$H(t) = (m^\dagger, b^\dagger) \begin{bmatrix} \frac{\Delta(t)}{2} & g(t) \\ g(t) & -\frac{\Delta(t)}{2} \end{bmatrix} \begin{pmatrix} m \\ b \end{pmatrix}. \quad (22)$$

It is isomorphic to the Hamiltonian $H(t) = \Delta(t)\sigma_z + g(t)\sigma_x$, for which the counterdiabatic term can be written as $\dot\theta\sigma_y$ [36]. In a state-resolved way, we demonstrate a transparent and rigorous connection between the original presentation [38] and the operator presentation in Eq. (19).

By virtue of the definitions in Eqs. (12) and (13), the adiabatic path from $|k\rangle_m|0\rangle_b$ to $|0\rangle_m|k\rangle_b$ under the total Hamiltonian (20) can be constructed as

$$|k(t)\rangle = |\epsilon_k(t)\rangle = \frac{1}{\sqrt{k!}}(A^\dagger)^k|0\rangle = |\epsilon_k\rangle \quad (23)$$

under the boundary conditions $\theta(t=0)=0$ and $\theta(t=T)=\pi/2$. And the system wave function can be written as

$$|\psi_k(t)\rangle = e^{-i\chi_k(t)}|k(t)\rangle, \quad (24)$$

where the quantum phase is

$$
\begin{aligned}
\chi_k(t) &= \int_0^t dt' E_k(t') - i \int_0^t dt' \langle\epsilon_k(t')|\partial_{t'}\epsilon_k(t')\rangle \\
&= \int_0^t dt' E_k(t') = k\chi(t).
\end{aligned} \quad (25)
$$

Here $E_k(t)$ is the instantaneous eigenvalue of eigenvector $|\epsilon_k\rangle$, $\langle\epsilon_k(t')|\partial_{t'}\epsilon_k(t')\rangle = 0$, and $\chi(t) \equiv \int_0^t dt' \omega_A(t')$.

Alternatively, by setting $\theta(0) = \pi/2$ and $\theta(T) = 0$, the adiabatic path followed by the system can be constructed as $|k(t)\rangle = |\epsilon_0(t)\rangle = (B^\dagger)^k|0\rangle/\sqrt{k!}$. To be self-consistent, we stick to the boundary conditions $\theta(0) = 0$ and $\theta(T) = \pi/2$ in this work.
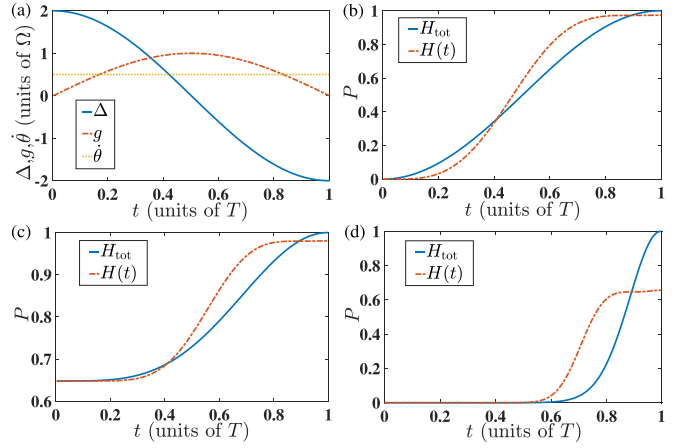

FIG. 2. (a): The time dependence of the driving-enhanced coupling strength g, the effective frequency of the lower-frequency hybrid mode Δ, and the time derivative of the control parameter $\dot\theta$, in units of the coupling strength $\Omega = \pi/T$. (b)–(d) The target-state population of the phonon mode b for the initial state of the hybrid mode m prepared as the Fock state $|n=4\rangle$, the cat state with $\zeta = 1$, and the cat state with $\zeta = 4$, respectively.

In general situations, a superposed state $|\psi(0)\rangle = \sum_k C_k |k0\rangle$ with normalized coefficients C_k will evolve adiabatically to

$$|\psi(T)\rangle = \sum_k C_k e^{-i\chi_k(T)}|0k\rangle \quad (26)$$

at the desired moment T along the path in Eq. (23). C_k is invariant with time. The quantum phase $\chi_k(T)$ for the Fock state with k excitations is proportional to k. Due to the preceding analysis, the local phase difference can be periodically compensated by the bare Hamiltonian of the mechanical mode. The state transfer thus has, indeed, been completed by Eq. (26).

Now we can verify the TQD approach in the state transfer from mode m to mode b by presenting the practical dynamics of the target-state population P given in Eq. (9). By setting the time dependence of the effective frequency Δ and the driving-enhanced coupling strength g to be in a sinusoid shape and using Eq. (21), we have

$$\Delta = 2\Omega\cos(2\theta), \quad g = \Omega\sin(2\theta), \quad \theta = \frac{\pi}{2}\frac{t}{T}, \quad (27)$$

where Ω is the coupling strength determined by the desired transfer time T as $\Omega T = \pi$. The shape functions of Δ, g, and $\dot\theta$ are plotted in Fig. 2(a). With various initial states of mode m, the blue solid lines and the red dot-dashed lines in Figs. 2(b)–2(d) describe the dynamics of the target-state population under $H_{\rm tot}$ in Eq. (20) with the counterdiabatic term and that under $H(t)$ in Eq. (7) without the counterdiabatic term, respectively.

One can find that practically, the accelerated state transfer could be perfectly completed by the TQD approach for both the Fock state and the superposed state. The latter is an even cat state $(|\zeta\rangle + |-\zeta\rangle)/\sqrt{2 + 2e^{-2\zeta^2}}$, where $|\zeta\rangle$ is the Glauber coherent state. For the Fock-state transfer $|4\rangle_m|0\rangle_b \rightarrow |0\rangle_m|4\rangle_b$ in Fig. 2(b), $P(T)$ approaches 0.90 using the original

Hamiltonian $H(t)$. Figures 2(c) and 2(d) for the cat states with $\zeta = 1$ and 4 show that $P(T)$ under the original Hamiltonian approaches 0.98 and 0.65, respectively. Thus, the TQD approach manifests its power for a larger cat state by achieving a perfect transfer population.

B. Invariant-based inverse engineering

Another mainstream accelerated adiabatic passage is invariant-based inverse engineering [36,41], where the parametrical adiabatic path of the system is designed through a Hermitian operator $I(t)$ termed the Levis-Riesenfeld invariant. For an arbitrary time-dependent Hamiltonian $H(t)$, the invariant satisfies

$$\frac{\partial I(t)}{\partial t} = -i[H(t), I(t)]. \tag{28}$$

In the framework of invariant-based inverse engineering, the wave function of a time-dependent Schrödinger equation $i\partial_t|\psi(t)\rangle = H(t)|\psi(t)\rangle$ can be expressed as $|\psi(t)\rangle = \sum_k C_k e^{-i\kappa_k(t)}|\epsilon_k(t)\rangle$, where C_k is a time-independent amplitude, $|\epsilon_k(t)\rangle$ is the eigenstates of the invariant $I(t)$, and κ_k is the Lewis-Riesenfeld phase, defined by

$$\dot{\kappa}_k(t) = \langle \epsilon_k(t)|[-i\partial_t + H(t)]|\epsilon_k(t)\rangle. \tag{29}$$

To ensure the desired state transfer rather than the full-time adiabatic passage, $I(t)$ and $H(t)$ have to share the same eigenstates at both ends of the passage.

To carry out the derivation of a general LR invariant for our two-coupled-resonator system with an arbitrary target state, we rewrite the system Hamiltonian $H(t)$ (7) as

$$H(t) = \frac{\Delta(t)}{2}m^\dagger m + [g_R(t) - ig_I(t)]m^\dagger b \\ + [g_R(t) + ig_I(t)]mb^\dagger - \frac{\Delta(t)}{2}b^\dagger b, \tag{30}$$

where $g_R(t)$ and $g_I(t)$ represent the real and imaginary parts of the complex coupling strength $g(t)$, respectively.

The corresponding Lewis-Riesenfeld invariant is formulated as

$$I(t) = \cos\beta(m^\dagger m - b^\dagger b) + \sin\beta(e^{-i\alpha}m^\dagger b + e^{i\alpha}mb^\dagger) \\ = A^\dagger A - B^\dagger B, \tag{31}$$

where

$$A = \cos\left(\frac{\beta}{2}\right)e^{\frac{i\alpha}{2}}m + \sin\left(\frac{\beta}{2}\right)e^{-\frac{i\alpha}{2}}b, \\ B = \sin\left(\frac{\beta}{2}\right)e^{\frac{i\alpha}{2}}m - \cos\left(\frac{\beta}{2}\right)e^{-\frac{i\alpha}{2}}b \tag{32}$$

are the normalized annihilation operators for $I(t)$ and both $\beta \equiv \beta(t)$ and $\alpha \equiv \alpha(t)$ are time-dependent functions to be determined. Substituting Eq. (31) into Eq. (28), we have

$$\dot{\beta} = 2g_I \cos\alpha - 2g_R \sin\alpha, \\ \dot{\alpha} = \Delta - \cot\beta(2g_R \cos\alpha + 2g_I \sin\alpha). \tag{33}$$

With the annihilation and creation operators in $I(t)$, the original Hamiltonian (30) can be rewritten as

$$H = \omega(A^\dagger A - B^\dagger B) + g_{AB}A^\dagger B + g_{AB}^* B^\dagger A, \tag{34}$$

where

$$\omega \equiv \frac{\Delta \cos\beta}{2} + g_R \sin\beta \cos\alpha + g_I \sin\beta \sin\alpha, \\ g_{AB} \equiv \frac{\Delta \sin\beta}{2} - g_R(\cos\beta \cos\alpha + i\sin\alpha) \\ - g_I(\cos\beta \sin\alpha - i\cos\alpha). \tag{35}$$

Then in the subspace with a fixed excitation number N, the general solution of the Schrödinger equation can be expressed as a superposition of the eigenstates of the invariant,

$$|\psi_N(t)\rangle = \sum_{n=0}^{N} p_n |\epsilon_{N-n}\rangle e^{-i\kappa_{N-n}(t)}, \tag{36}$$

where p_n is a normalized coefficient; $|\epsilon_{N-n}\rangle$ is the normalized eigenstates of the LR invariant, taking the same form as in Eq. (13); and $\kappa_{N-n}(t)$ is the LR phase defined in Eq. (29).

We first consider the state transfer from $|N\rangle_m|0\rangle_b$ to $|0\rangle_m|N\rangle_b$. With the definitions in Eqs. (32) and (13), one can construct a particular solution via

$$|\psi_N(t)\rangle = |\epsilon_N\rangle e^{-i\kappa_N(t)} = \frac{e^{-i\kappa_N(t)}}{\sqrt{N!}}(A^\dagger)^N|0\rangle \tag{37}$$

under the boundary conditions $\beta(0) = 0$ and $\beta(T) = \pi$. As for the Lewis-Riesenfeld phase, we have

$$\dot{\kappa}_N = -i\langle \epsilon_N|\partial_t|\epsilon_N\rangle + \langle \epsilon_N|H|\epsilon_N\rangle \\ = -i\left(-iN\frac{\dot{\alpha}\cos\beta}{2}\right) + N\frac{\Delta\cos\beta}{2} \\ + N(g_R \sin\beta \cos\alpha + g_I \sin\beta \cos\alpha) \\ = N\frac{g_R \cos\alpha + g_I \sin\alpha}{\sin\beta} = N\dot{\kappa}, \tag{38}$$

with $\dot{\kappa} \equiv (g_R \cos\alpha + g_I \sin\alpha)/\sin\beta$, where we have applied the time derivative of operators A and B,

$$\frac{\partial}{\partial t}A^\dagger = -\frac{\dot{\beta}}{2}B^\dagger - \frac{i\dot{\alpha}}{2}(\cos\beta A^\dagger + \sin\beta B^\dagger), \\ \frac{\partial}{\partial t}B^\dagger = \frac{\dot{\beta}}{2}B^\dagger - \frac{i\dot{\alpha}}{2}(\sin\beta A^\dagger - \cos\beta B^\dagger), \tag{39}$$

and Eqs. (33) and (34).

Given the time-dependent parameters $\beta(t)$, $\alpha(t)$, and $\kappa(t)$ in Eqs. (33) and (38), the coupling strengths and the effective frequency of the hybrid mode that are directly used in quantum control are expressed as

$$g_R = \dot{\kappa} \cos\alpha \sin\beta - \frac{\dot{\beta}}{2}\sin\alpha, \\ g_I = \dot{\kappa} \sin\alpha \sin\beta + \frac{\dot{\beta}}{2}\cos\alpha, \\ \Delta = \dot{\alpha} + 2\dot{\kappa}\cos\beta. \tag{40}$$

By virtue of their excitation-number independence, we can further consider the transfer of an arbitrary superposed state from mode m to mode b under the same boundary conditions. Thus, in a general situation, an initial state

$$|\psi(0)\rangle = \sum_k C_k |k0\rangle = \sum_k C_k |\psi_k(0)\rangle, \tag{41}$$
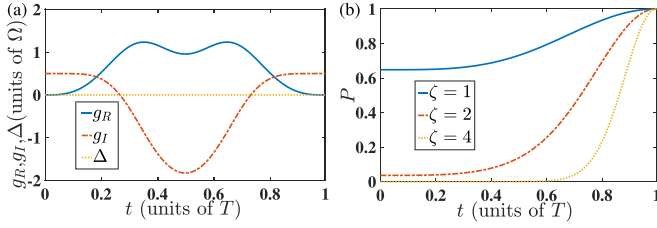
FIG. 3. (a) The shapes of the real and imaginary parts of the driving-enhanced coupling strength g_R and g_I and the effective frequency of the hybrid mode Δ, in units of the coupling strength $\Omega = \pi/T$. (b) The dynamics of the state population of mode b under various initial cat states of the hybrid mode m. Here the control parameters are set as $\beta = \pi t/T$, $\alpha = -4/3\sin^3\beta$, and $\kappa = \beta - \sin(2\beta)/2$.

where C_k is the time-independent normalized coefficient for the number state $|k\rangle$, will evolve to

$$|\psi(T)\rangle = \sum_k C_k e^{-ik(\kappa+\alpha)}|0k\rangle \qquad (42)$$

at the final time T, according to Eqs. (37) and (32).

The state transfer assisted by the Lewis-Riesenfeld invariant can be verified in Fig. 3 by the state population P of phonon mode b given in Eq. (9). With the selected control functions of β, α, and κ, one can find the time dependence of the real and imaginary parts of the coupling strength g_R and g_I and the frequency of the hybrid mode Δ through Eq. (40), as plotted in Fig. 3(a). The initial states in Fig. 3(b) are various cat states with $\zeta = 1, 2, 4$. It is found that a perfect transfer for a superposed state can always be achieved via the LR-invariant-based inverse engineering.

IV. STATE TRANSFER UNDER SYSTEMATIC ERRORS

In practice, the ideal trajectory of the control parameters cannot be exactly implemented because of the technical imperfections and constraints. These systematic errors pose the need for studying the perturbation effect on transport protocols and optimizing protocols that are robust with respect to the stochastic fluctuation in the Hamiltonian [54]. In this section, the Hamiltonian implemented in experiments is assumed to be

$$H_{\exp} = H(t) + \gamma H_g + \eta H_\Delta, \qquad (43)$$

where $H(t) = H_g + H_\Delta$ is the ideal or unperturbed Hamiltonian in Eq. (7) and H_g and H_Δ are, respectively, the interaction Hamiltonian between the hybrid mode and the phonon mode and the bare Hamiltonian, i.e.,

$$\begin{aligned} H_g &\equiv g(t)m^\dagger b + g^*(t)mb^\dagger, \\ H_\Delta &\equiv \frac{\Delta(t)}{2}(m^\dagger m - b^\dagger b). \end{aligned} \qquad (44)$$

γ and η are dimensionless perturbation coefficients for the coupling strength and the frequency detuning, respectively.

With the practical Hamiltonian (43), the evolved state is obtained from the Schrödinger equation

$$i\frac{\partial}{\partial t}|\Psi(t)\rangle = [H(t) + \gamma H_g + \eta H_\Delta]|\Psi(t)\rangle. \qquad (45)$$

Then the sensitivity to the systematic error is defined as

$$q_g = -\frac{\partial P(T)}{\partial(\gamma^2)}\bigg|_{\gamma=0}, \qquad q_\Delta = -\frac{\partial P(T)}{\partial(\eta^2)}\bigg|_{\eta=0}, \qquad (46)$$

where $P(T)$ is the state population evaluated by replacing the evolved state in Eq. (9) with $|\Psi(T)\rangle$ at the final time T. We write $P(T)$ as P for simplicity in Secs. IV A, IV B, and IV C.

A. π pulse

Before working on the two accelerated adiabatic passages, we first consider a straightforward π pulse for the state transfer. Then in Eq. (7), it is found that $\Delta(t) = 0$ and $\int_0^T dt\, g(t) = \pi/2$. Accordingly, Eq. (43) becomes $H_{\exp} = (1+\gamma)H_g$, which can be diagonalized with the normalized operators $A = (m+b)/\sqrt{2}$ and $B = (m-b)/\sqrt{2}$, similar to the transformation in Eqs. (11) and (12). The special initial state $|\Psi(0)\rangle = |N\rangle_m|0\rangle_b = |N0\rangle$ can then be expanded by the eigenstates in Eq. (13),

$$|N0\rangle = \frac{1}{\sqrt{2^N}}\sum_{n=0}^N \sqrt{C_N^n}|\epsilon_{N-n}\rangle, \qquad (47)$$

where $C_N^n = N!/n!/(N-n)!$. The eigenvalue of $|\epsilon_{N-n}\rangle$ is now $(N-2n)(1+\gamma)g(t)$ due to $H_{\exp}$. So we have

$$|\Psi(T)\rangle = \frac{1}{\sqrt{2^N}}\sum_{n=0}^N \sqrt{C_N^n}e^{-i(N-2n)(1+\gamma)\frac{\pi}{2}}|\epsilon_{N-n}\rangle, \qquad (48)$$

using the Schrödinger equation (45). According to Eqs. (11) and (12), the target state reads

$$|0N\rangle = \frac{1}{\sqrt{2^N}}\sum_{n=0}^N (-1)^n\sqrt{C_N^n}|\epsilon_{N-n}\rangle. \qquad (49)$$

Then the transfer fidelity measured by the target-state population P in mode b is

$$P = |\langle 0N|\Psi(T)\rangle|^2 = \cos^{2N}\left(\frac{\pi}{2}\gamma\right) \qquad (50)$$

by virtue of Eq. (9). And from Eq. (46), the systematic-error sensitivity to the coupling strength for the Fock state $|N0\rangle$ is

$$q_g = \frac{N\pi^2}{4}. \qquad (51)$$

The preceding derivation can be straightforwardly extended to an arbitrary superposed state $|\psi(0)\rangle = \sum_k C_k|k0\rangle$ by virtue of its independence from the excitation number. Then in general situations, we have

$$\begin{aligned} P &= \sum_{C_k\neq 0} |C_k|^2 \cos^{2k}\left(\frac{\pi}{2}\gamma\right), \\ q_g &= \frac{\pi^2}{4}\sum_{C_k\neq 0} k|C_k|^2 = \frac{\pi^2}{4}\bar{n}_m. \end{aligned} \qquad (52)$$

It is interesting to find that the systematic-error sensitivity in the π-pulse protocol is proportional to the average excitation number $\bar{n}_m$ of the initial state. In contrast to the constant result in Ref. [54] for a two-level system, this indicates that the continuous-variable system is more fragile without the assistance from the counterdiabatic field or the inverse engineering.
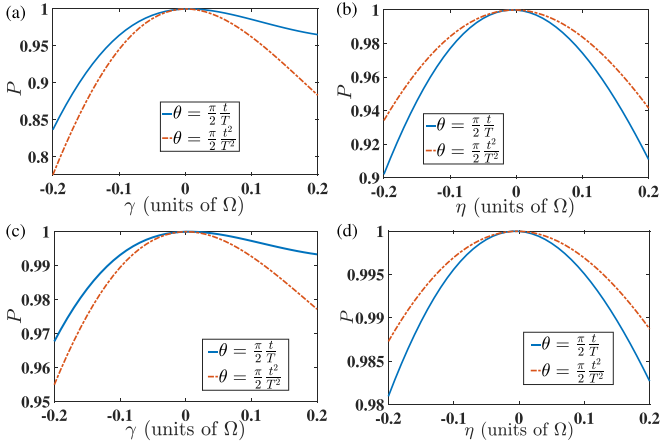
FIG. 4. State-transfer population $P(T)$ of the phonon mode b as a function of the systematic errors associated with the coupling strength γ or the frequency detuning η for various target states and shape functions of the TQD protocol. In (a) and (b), the initial state is the Fock state $|4\rangle$, and in (c) and (d), it is the cat state with $\zeta = 1$. $T = \pi/\Omega$.

FIG. 5. State-transfer population $P(T = \pi/\Omega)$ of the phonon mode b in the space of the systematic-error parameters γ and η. The target state is chosen as the cat state with $\zeta = 1$.

From the results for various initial states and sources of errors in Figs. 4 and 5, the state-transfer fidelity can be maintained above 0.95 with up to 10% fluctuations in the system parameters. One can generally find that the TQD approach is robust against the systematic errors.

B. Transitionless quantum driving

Now we analyze the stability of the state transfer and error sensitivity of the TQD protocol provided in Sec. III A. Note that the unperturbed Hamiltonian $H(t)$ in the total Hamiltonian (20) is replaced by $H_{\rm exp}$ in Eq. (43). In Fig. 4, the TQD protocols are carried out using the time dependence of the effective frequency $\Delta(t)$ and the driving-enhanced coupling strength $g(t)$ (assumed to be real for TQD), which are determined by the shape functions of $\theta = \pi/2(t/T)$ (see the blue solid lines) or $\theta = \pi/2(t/T)^2$ (see the red dot-dashed lines). In Figs. 4(a) and 4(c) $\eta = 0$, and in Figs. 4(b) and 4(d) $\gamma = 0$. One can observe that the protocol stability is not sensitive to the choice of target states. It is found that the impact of the coupling-strength fluctuation of the interaction Hamiltonian H_g is asymmetrical to the parameter γ in the negative and positive axes. With the same magnitude, the decrement in the state population P induced by a positive γ is clearly smaller than that induced by a negative γ. In particular, $P = 0.92$ for $\gamma/\Omega = 0.2$, and $P = 0.84$ for $\gamma/\Omega = -0.2$. In contrast, the state-transfer population is roughly symmetrical to the energy fluctuation η of the free Hamiltonian H_Δ. Another difference between Figs. 4(a) and 4(b) or between Figs. 4(c) and 4(d) manifests in the error sensitivity to the shape of the control parameter $\theta(t)$. For a nonvanishing γ (η), the protocol is more robust with the linear function $\theta = \pi/2(t/T)$ [the quadratic function $\theta = \pi/2(t/T)^2$] than that with the quadratic function $\theta = \pi/2(t/T)^2$ [the linear function $\theta = \pi/2(t/T)$].

In Fig. 5, we switch on simultaneously the systematic error in both the interaction Hamiltonian and free Hamiltonian and fix the target state as a cat state with $\zeta = 1$. As expected, a nearly unity state transfer is found in a remarkable regime around $\gamma \approx \eta$. It can be readily understood that when $\gamma \approx \eta$, the experimental Hamiltonian $H_{\rm exp}$ in Eq. (43) is approximated by $(1 + \gamma)H(t)$, equivalent to a rescaling over the whole original Hamiltonian that renders the same counterdiabatic Hamiltonian $H_{\rm CD}$ in Eq. (19).
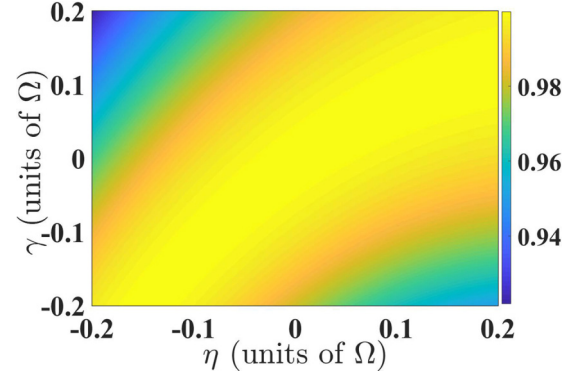
C. Invariant-based inverse engineering

In this section, we construct an optimal protocol against the systematic errors by using the Lewis-Riesenfeld invariant in Eq. (31). Now we employ the ideal Hamiltonian $H(t)$ in Eq. (30) with a complex coupling strength $g(t)$. The ideal evolution operator reads

$$U_0(s, t) = \sum_{n=0}^{N} e^{-i(N-2n)[\kappa(s)-\kappa(t)]} |\epsilon_{N-n}(s)\rangle\langle\epsilon_{N-n}(t)|. \quad (53)$$

Under the assumption that the initial state is $|N\rangle_m|0\rangle_b$ and by virtue of Eqs. (36) and (37), the unperturbed solution reads

$$|\psi(t)\rangle = |\epsilon_N(t)\rangle e^{-iN\kappa(t)}, \quad (54)$$

where κ is defined in the last line of Eq. (38). Considering the practical Schrödinger equation in Eq. (45), the final-state population (up to the second order of γ and η) is

$$P \approx 1 - \gamma^2 \sum_{n=1}^{N} \left| \int_0^T dt\, e^{-2ni\kappa(t)} \langle\epsilon_{N-n}(t)|H_g|\epsilon_N(t)\rangle \right|^2$$
$$- \eta^2 \sum_{n=1}^{N} \left| \int_0^T dt\, e^{-2ni\kappa(t)} \langle\epsilon_{N-n}(t)|H_\Delta|\epsilon_N(t)\rangle \right|^2. \quad (55)$$

By virtue of

$$\langle\epsilon_{N-1}(t)|H_g|\epsilon_N(t)\rangle = -\sqrt{N}\dot{\kappa}\sin\beta\cos\beta + \frac{i\sqrt{N}\dot{\beta}}{2},$$
$$\langle\epsilon_{N-n}(t)|H_g|\epsilon_N(t)\rangle = 0, \quad n \neq 1,$$
$$\langle\epsilon_{N-1}(t)|H_\Delta|\epsilon_N(t)\rangle = \frac{\sqrt{N}\dot{\alpha}}{2}\sin\beta + \sqrt{N}\dot{\kappa}\sin\beta\cos\beta,$$
$$\langle\epsilon_{N-n}(t)|H_\Delta|\epsilon_N(t)\rangle = 0, \quad n \neq 1, \quad (56)$$

and the boundary conditions $\beta(0) = 0$ and $\beta(0) = \pi$, the systematic-error sensitivities for $|\psi(0)\rangle = |N0\rangle$ are found to

be

$$q_g = N \left| \int_0^T dt\, \dot{\beta} \sin^2 \beta\, e^{-2i\kappa} \right|^2,$$

$$q_\Delta = N \left| \int_0^T dt\, \sin \beta \left(\frac{\dot{\alpha}}{2} + \dot{\kappa} \cos \beta \right) e^{-2i\kappa} \right|^2, \quad (57)$$

according to Eq. (46). When κ is constant, we restore the result in the π-pulse case $q_g = N\pi^2/4$, irrespective of the shape of $\beta(t)$.

It is interesting to find that $q_g = 0$ can be attained when

$$\kappa(t) = j \left[\beta - \frac{\sin(2\beta)}{2} \right] \quad (58)$$

with a nonzero integer j. And $q_\Delta = 0$ can be attained when

$$\frac{\dot{\alpha}}{2} + \dot{\kappa} \cos \beta = 0. \quad (59)$$

Equations (58) and (59) render $\dot{\alpha} = -4j\dot{\beta} \cos^2 \beta \sin \beta$. An immediate choice is $\alpha = -4j \cos^3 \beta / 3$. Therefore, the invariant-based inverse engineering complemented by optimization that is robust against the systematic errors is described by

$$\beta(0) = 0, \quad \beta(T) = \pi,$$
$$\kappa(t) = j \left[\beta - \frac{\sin(2\beta)}{2} \right], \quad (60)$$
$$\alpha(t) = -\frac{4j \cos^3 \beta}{3}.$$

Consequently, the control protocol in Eq. (40) turns out to be

$$g_R = 2\dot{\beta} \sin^3 \beta \cos \left(\frac{4}{3} \sin^3 \beta \right) + \frac{\dot{\beta}}{2} \sin \left(\frac{4}{3} \sin^3 \beta \right),$$

$$g_I = -2\dot{\beta} \sin^3 \beta \sin \left(\frac{4}{3} \sin^3 \beta \right) + \frac{\dot{\beta}}{2} \cos \left(\frac{4}{3} \sin^3 \beta \right), \quad (61)$$

$$\Delta = 0,$$

where we have set $j = 1$. More importantly, the optimized protocol in Eq. (61) and the parametric setting in Eq. (60) are independent of the excitation number. Thus, they apply to a general superposed state $|\psi(0)\rangle = \sum_k C_k |k0\rangle$ across the whole Hilbert space. The fidelity is found to be

$$P = 1 - \gamma^2 \sum_{C_k \neq 0} |C_k|^2 \left| \int_0^T dt \langle \epsilon_{k-1}(t) | H_g | \epsilon_k(t) \rangle \right|^2. \quad (62)$$

Note that in Eq. (61), $\Delta = 0$ implies that P is strictly insensitive to η.

In Fig. 6, we compare the systematic-error sensitivities under various state-transfer protocols, including the flat π pulse (blue solid lines), the transitionless quantum driving protocol described by the parametric functions in Eq. (27) (red dot-dashed lines), and the optimized protocol based on the LR invariant described by Eq. (61) (orange dotted lines). It is found that for both the Fock state and the cat state, the optimized protocol assisted by the LR invariant demonstrates a much stronger robustness than the TQD protocol. In particular, in the range of the normalized coupling error
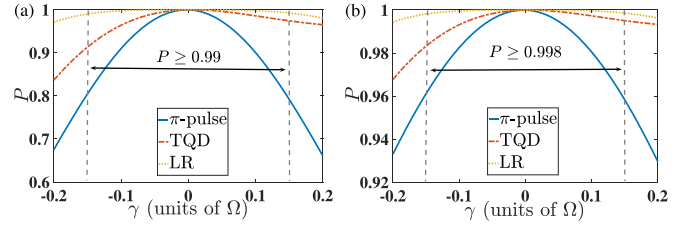

FIG. 6. State-transfer population $P(T = \pi/\Omega)$ of the phonon mode b as a function of the systematic errors associated with the coupling strength γ for various protocols. The initial state in (a) is the Fock state $|4\rangle$, and in (b) it is the cat state with $\zeta = 1$.

$-0.15 \leqslant \gamma/\Omega \leqslant 0.15$, the transfer fidelity can be maintained as $P \geqslant 0.99$ and $P \geqslant 0.998$ for the Fock state and the cat state, respectively. The flat π pulse behaves as the most fragile protocol.

An important common point shared by Figs. 4 and 6 is that the robustness of these state-transfer protocols to the systematic errors is weakened by the average excitation number of the target state. This is consistent with the result for the π-pulse transfer in Eq. (52).

V. DISCUSSION

Alternatively, the robustness of the state-transfer protocols can be tested by taking the effects of dissipative thermal baths into account. Given the weak system-bath interaction in cavity magnomechanical systems [9,22], we calculate the transfer population with the standard Lindblad master equation under the Born-Markovian approximation. The dynamical equation reads

$$\frac{\partial \rho(t)}{\partial t} = -i[H(t), \rho(t)]$$
$$+ [\kappa_m(\bar{n}_m + 1)L(m) + \kappa_m \bar{n}_m L(m^\dagger)]\rho$$
$$+ [\kappa_b(\bar{n}_b + 1)L(b) + \kappa_b \bar{n}_b L(b^\dagger)]\rho, \quad (63)$$

where the superoperation for any Lindblad operator o, $o = m, b$, is defined as

$$L(o)\rho \equiv o\rho o^\dagger - \frac{1}{2} o^\dagger o \rho - \frac{1}{2} \rho o^\dagger o. \quad (64)$$

Here ρ is the density operator of the two modes, and $H(t)$ is the system Hamiltonian in Eq. (20) for the TQD protocol or that in Eq. (30) for the invariant protocol. κ_m and κ_b represent the decay rates of the hybrid mode m and phonon mode b, respectively. In the numerical evaluation, we choose the mode frequencies to be $\omega_m/2\pi = 10$ GHz and $\omega_b/2\pi = 10$ MHz and the damping rates to be $\kappa_b = 100$ Hz and $\kappa_m = 10$ kHz [9,22]. The two thermal baths are assumed to have a common temperature T_{th}; then the average excitation number for mode o is $\bar{n}_o = [\exp(\omega_o/k_B T_{\text{th}}) - 1]^{-1}$. The evolution time is fixed as $\Omega T = \pi$, with $\Omega/2\pi = 1$ MHz.

The transfer population defined in Eq. (9) for a special cat state at various temperatures is plotted in Fig. 7. Comparing Figs. 7(a) and 7(b), we see that the influences from the thermal baths are almost the same for both protocols of accelerated adiabatic passage, i.e., TQD and invariant STA. The transfers are found to be robust against the thermal baths with low temperatures. $P(T)$ can be maintained above 0.97 when
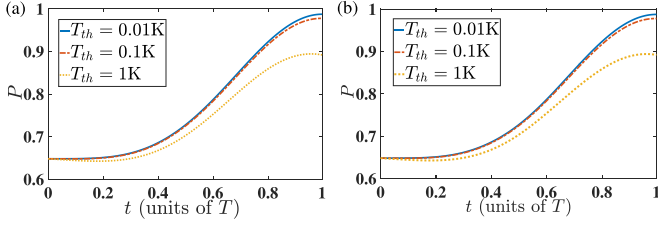
FIG. 7. The dynamics of the target-state population in mode b in the presence of thermal baths with various temperatures. In (a) we use the TQD protocol as described in Fig. 2, and in (b) we use the LR-invariant protocol as described in Fig. 3. Here the initial state is set as the cat state with $\zeta = 1$.

$T_{\text{th}} \leqslant 0.1$ K. Even under a comparative high-temperature, e.g., $T_{\text{th}} = 1$ K, the population is still above 0.88.

Our proposals are based on the system Hamiltonian (7) under the rotating-wave approximation. Omitting the counterrotating terms means the coupling strength g has to be kept much smaller than the eigenfrequency ω_b. However, $g \ll \omega_b$ might be violated during any accelerated adiabatic passage. To consider the effect of the counterrotating terms, we should go back to the linearized Hamiltonian in Eq. (A8) with two hybrid modes and a phonon mode. After the unitary transformation with respect to $U(t) = \exp[i \int_0^t ds \Delta'(s) a^\dagger a]$, we have

$$
\begin{aligned}
H = {}& \Delta m^\dagger m + \omega_b b^\dagger b + g(m^\dagger b + m^\dagger b^\dagger) + g^*(mb^\dagger + mb) \\
& + g'\{a^\dagger b e^{i[\int_0^t ds \Delta'(s)]} + a^\dagger b^\dagger e^{i[\int_0^t ds \Delta'(s)]}\} \\
& + g'^*\{ab^\dagger e^{-i[\int_0^t ds \Delta'(s)]} + ab e^{-i[\int_0^t ds \Delta'(s)]}\}.
\end{aligned}
\tag{65}
$$

Discarding the fast-oscillating terms and using the same conventions as in Eq. (6), the Hamiltonian turns out to be

$$
\begin{aligned}
H = {}& [\omega_b + \Delta(t)]m^\dagger m + \omega_b b^\dagger b \\
& + g(t)m^\dagger(b + b^\dagger) + g^*(t)m(b + b^\dagger).
\end{aligned}
\tag{66}
$$

Note it can be further reduced to the Hamiltonian (7) under a rotating-wave approximation with a sufficiently large ω_b.

Figure 8 demonstrates the effect of the counterrotating terms under various transfer protocols and target states. The TQD protocol and the invariant protocol use the same parameters as in Figs. 2(a) and 3(a), respectively. The transfer populations for the Fock state $|n = 1\rangle$ and the superposed state, i.e., the cat state with $\zeta = 1$, are presented, respectively, in Figs. 8(a)–8(d). Figures 8(a) and 8(c) show that the counterrotating Hamiltonian can be omitted for STA protocols with a sufficiently large ω_b. When $\omega_b/\Omega = 10$, even the population under the π-pulse protocol deviates slightly from the unit transfer. When ω_b decreases to $\omega_b/\Omega = 4$, it is interesting to find in Figs. 8(b) and 8(d) that the optimized invariant-based protocol renders the most disappointing result among the three protocols. In particular, when the initial state is the Fock state $|1\rangle_m|0\rangle_b$, P becomes even smaller than 0.2. Yet the performance of the TQD protocol is still perfect, showing great robustness to the presence of the counterrotating interactions.
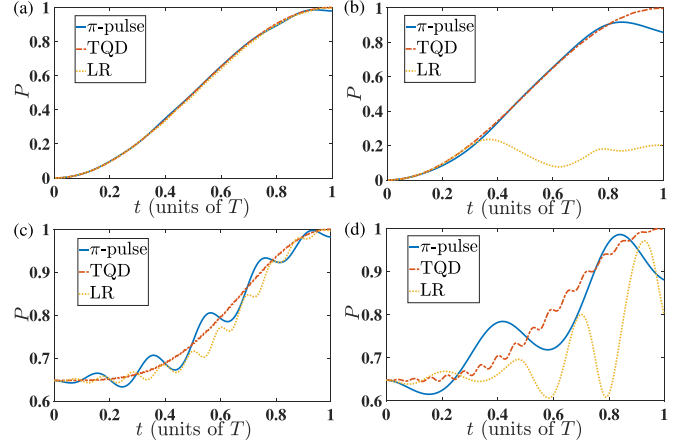

FIG. 8. The population dynamics in the presence of the counterrotating interaction for various state-transfer protocols. In (a) and (b), the initial state is the Fock state $|1\rangle$, and in (c) and (d), it is the cat state with $\zeta = 1$. The phonon-mode frequency is set as $\omega_b/\Omega = 10$ in (a) and (c) and as $\omega_b/\Omega = 4$ in (b) and (d). $\Omega T = \pi$.

VI. CONCLUSION

In summary, we have applied two shortcut-to-adiabatic protocols to the cavity magnomechanical system to realize a fast-and-faithful transfer for arbitrary states, where the magnon mode is simultaneously coupled to a microwave cavity mode and the mechanical-vibration mode in the same YIG sphere. Our work demonstrates how to construct the counterdiabatic Hamiltonian in terms of the creation and annihilation operators in a state-resolved way, which explicitly shows two evolution paths or quantum trajectories in the state space. We derived in detail the Levis-Riesenfeld invariant, based on which inverse engineering of arbitrary initial states of the continuous-variable systems can be performed. In terms of the systematic error, we obtained the optimized regimes or conditions for both the TQD protocol and LR-invariant-based protocol. The LR protocol outperforms the TQD protocol with the same systematic error in the coupling strength. However, the TQD protocol overwhelms the LR protocol in the presence of counterrotating interactions. The robustness of both protocols to the systematic error declines with the average excitation number of the target state. We also estimated the upper bound of the bath temperature under which these protocols can be implemented in the cavity magnomechanical system.

Our work in pursuit of quantum state transfer and protection provides an important application of the hybrid magnomechanical system as a promising hybrid platform for real-time control. It also applies to constructing accelerated adiabatic passages in a general continuous-variable system.

APPENDIX: EFFECTIVE HAMILTONIAN FOR STATE TRANSFER IN THE HYBRID MAGNOMECHANICAL SYSTEM

This Appendix contributes to deriving the effective Hamiltonian (2) for state transfer in the cavity magnomechanical system in Fig. 1. With respect to the transformation $U = \exp[i\omega_p t(a_1^\dagger a_1 + m_1^\dagger m_1)]$, the original Hamiltonian in Eq. (1) turns out to be

$$
\begin{aligned}
H_0 &= \Delta_a a_1^\dagger a_1 + \Delta_m m_1^\dagger m_1 + \omega_b b^\dagger b + g_{ma}(a_1 m_1^\dagger + a_1^\dagger m_1) \\
&\quad + g_{mb} m_1^\dagger m_1 (b + b^\dagger) + i(\epsilon_p a_1^\dagger - \epsilon_p^* a_1),
\end{aligned} \tag{A1}
$$

where $\Delta_a = \omega_a - \omega_p$ and $\Delta_m = \omega_m - \omega_p$. In the strong-coupling regime for the magnon-photon interaction, we have $g_{ma} \gg \kappa_1, \kappa_2$, where κ_1 and κ_2 represent the decay rates of the photon and magnon, respectively. The magnon mode, i.e., the collective spin-wave excitations, can efficiently interface with microwave photons, thereby consolidating the strength of the dispersive interaction to produce well-separated hybridized modes. These dressed normal modes read

$$
m = \sin\phi a_1 - \cos\phi m_1, \quad a = \cos\phi a_1 + \sin\phi m_1, \tag{A2}
$$

where $\tan(2\phi) \equiv 2g_{ma}/(\Delta_a - \Delta_m)$ and $\phi \in [0, \pi/2]$. Then the Hamiltonian of the hybrid photon-magnon-phonon system in Eq. (A1) can be rewritten as

$$
\begin{aligned}
H &= \Delta' a^\dagger a + \Delta m^\dagger m + \omega_b b^\dagger b \\
&\quad + i\epsilon_p(\cos\phi a^\dagger + \sin\phi m^\dagger) - i\epsilon_p^*(\cos\phi a + \sin\phi m) \\
&\quad + g_{mb}(b + b^\dagger)(\sin^2\phi a^\dagger a - \sin\phi \cos\phi a^\dagger m \\
&\quad - \sin\phi \cos\phi a m^\dagger + \cos^2\phi m^\dagger m),
\end{aligned} \tag{A3}
$$

with

$$
\begin{aligned}
\Delta &= \frac{\omega_a + \omega_m}{2} - \omega_p - \sqrt{\left(\frac{\omega_a - \omega_m}{2}\right)^2 + g_{ma}^2}, \\
\Delta' &= \frac{\omega_a + \omega_m}{2} - \omega_p + \sqrt{\left(\frac{\omega_a - \omega_m}{2}\right)^2 + g_{ma}^2}.
\end{aligned} \tag{A4}
$$

Due to the input-output theory or the Heisenberg-Langevin equation, the time evolution of the system operators satisfies

$$
\begin{aligned}
\dot{a} &= -(i\Delta' + \kappa_a)a + \epsilon_p \cos\phi - ig_{mb}\sin^2\phi a(b + b^\dagger) \\
&\quad - ig_{mb}\sin\phi \cos\phi m(b + b^\dagger) + \sqrt{2\kappa_a} a_{\text{in}}, \\
\dot{m} &= -(i\Delta + \kappa_m)m + \epsilon_p \sin\phi - ig_{mb}\cos^2\phi m(b + b^\dagger) \\
&\quad - ig_{mb}\sin\phi \cos\phi a(b + b^\dagger) + \sqrt{2\kappa_m} m_{\text{in}}, \\
\dot{b} &= -(i\omega_b + \kappa_b)b - ig_{mb}(\sin^2\phi a^\dagger a - \sin\phi \cos\phi a^\dagger m \\
&\quad - \sin\phi \cos\phi a m^\dagger + \cos^2\phi m^\dagger m) + \sqrt{2\kappa_b} b_{\text{in}}, \tag{A5}
\end{aligned}
$$

where $\kappa_a = \kappa_1 \cos^2\phi + \kappa_2 \sin^2\phi$, $\kappa_m = \kappa_1 \sin^2\phi + \kappa_2 \cos^2\phi$ [9], and κ_b are the decay rates of the modes a, m, and b, respectively.

The steady-state values $a_s \equiv \langle a \rangle$, $m_s \equiv \langle m \rangle$, and $b_s \equiv \langle b \rangle$ are determined by letting $\dot{a} = \dot{m} = \dot{b} = 0$. We have

$$
\begin{aligned}
&-(i\Delta' + \kappa_a)a_s + \epsilon_p \cos\phi - ig_{mb}a_s(b_s + b_s^*)\sin^2\phi \\
&\quad - ig_{mb}m_s(b_s + b_s^*)\sin\phi \cos\phi = 0, \\
&-(i\Delta + \kappa_m)m_s + \epsilon_p \sin\phi - ig_{mb}m_s(b_s + b_s^*)\cos^2\phi \\
&\quad - ig_{mb}a_s(b_s + b_s^*)\sin\phi \cos\phi = 0, \\
&-(i\omega_b + \kappa_b)b_s - ig_{mb}(|a_s|^2 \sin^2\phi - a_s^* m_s \sin\phi \cos\phi \\
&\quad - a_s m_s^* \sin\phi \cos\phi + |m_s|^2 \cos^2\phi) = 0. \tag{A6}
\end{aligned}
$$

Due to the fact that $g_{mb} \ll \omega_b$ [9], the last equation yields $b_s \approx 0$. Then we have

$$
m_s = \frac{\epsilon_p \sin\phi}{i\Delta + \kappa_m}, \quad a_s = \frac{\epsilon_p \cos\phi}{i\Delta' + \kappa_a}. \tag{A7}
$$

Following the standard linearization approach [8], we can rewrite the linearized Hamiltonian with the hybrid modes,

$$
\begin{aligned}
H &= \Delta' a^\dagger a + \Delta m^\dagger m + \omega_b b^\dagger b + (g' a^\dagger + g'^* a)(b + b^\dagger) \\
&\quad + (g m^\dagger + g^* m)(b + b^\dagger), \tag{A8}
\end{aligned}
$$

by substituting the steady-state values in Eq. (A7) into the Hamiltonian (A3) and ignoring all the high-order terms of fluctuations and operators. The coupling strengths turn out to be

$$
\begin{aligned}
g &= g_{mb}m_s \cos^2\phi - g_{mb}a_s \sin\phi \cos\phi, \\
g' &= g_{mb}a_s \sin^2\phi - g_{mb}m_s \sin\phi \cos\phi. \tag{A9}
\end{aligned}
$$

According to Eq. (A4), the two hybrid modes a (with a higher frequency) and m (with a lower frequency) are well-separated polaritonic modes, characterizing level repulsion by the strong magnon-photon coupling $\Delta' - \Delta \geqslant 2g_{ma} \gg \kappa_a, \kappa_m$. Then under either the blue-detuning driving (with a higher ω_p yielding negative Δ' and Δ) or the red-detuning driving (with a lower ω_p yielding positive Δ' and Δ), one can determine four different situations when exacting a pair of nearly resonant modes, m and b or a and b. It should be noted that our state-transfer approaches are applicable to all of them. Now we choose the situation under the red-detuning driving, and the higher-frequency hybrid mode is far off resonant from b; that is, we have $\Delta' - \omega_b \approx 2g_{ma}/\sin 2\phi \gg 0$.

Transforming the Hamiltonian (A8) into the interaction picture with respect to $U = \exp[i\int_0^t ds \Delta'(s) a^\dagger a + i\omega_b(m^\dagger m + b^\dagger b)t]$, we have

$$
\begin{aligned}
H &= (\Delta - \omega_b)m^\dagger m \\
&\quad + g'\{a^\dagger b e^{i[\int_0^t ds \Delta'(s) - \omega_b t]} + a^\dagger b^\dagger e^{i[\int_0^t ds \Delta'(s) + \omega_b t]}\} \\
&\quad + g'^*\{ab^\dagger e^{-i[\int_0^t ds \Delta'(s) - \omega_b t]} + ab e^{-i[\int_0^t ds \Delta'(s) + \omega_b t]}\} \\
&\quad + g(m^\dagger b + m^\dagger b^\dagger e^{2i\omega_b t}) + g^*(mb^\dagger + mb e^{-2i\omega_b t}). \tag{A10}
\end{aligned}
$$

After we discard the fast-oscillating terms, the Hamiltonian turns out to be

$$
H = (\Delta - \omega_b)m^\dagger m + (g m^\dagger b + g^* m b^\dagger). \tag{A11}
$$

That is exactly the effective Hamiltonian in Eq. (2) describing the lower-frequency hybrid mode coupled to the phonon mode.

[1] B. Z. Rameshti, S. V. Kusminskiy, J. A. Haigh, K. Usami, D. Lachance-Quirion, Y. Nakamura, C.-M. Hu, H. X. Tang, G. E. Bauer, and Y. M. Blanter, Cavity magnonics, arXiv:2106.09312.

[2] D. Lachance-Quirion, Y. Tabuchi, A. Gloppe, K. Usami, and Y. Nakamura, Hybrid quantum systems based on magnonics, Appl. Phys. Express **12**, 070101 (2019).

[3] Y. Li, W. Zhang, V. Tyberkevych, W. K. Kwok, and V. Novosad, Hybrid magnonics: Physics, circuits, and applications for coherent information processing, J. Appl. Phys. **128**, 130902 (2020).

[4] T. D. Ladd, F. Jelezko, R. Laflamme, Y. Nakamura, C. Monroe, and J. L. O'Brien, Quantum computers, Nature (London) **464**, 45 (2010).

[5] A. Reiserer and G. Rempe, Cavity-based quantum networks with single atoms and optical photons, Rev. Mod. Phys. **87**, 1379 (2015).

[6] C. L. Degen, F. Reinhard, and P. Cappellaro, Quantum sensing, Rev. Mod. Phys. **89**, 035002 (2017).

[7] A. Blais, A. L. Grimsmo, S. M. Girvin, and A. Wallraff, Circuit quantum electrodynamics, Rev. Mod. Phys. **93**, 025005 (2021).

[8] M. Aspelmeyer, T. J. Kippenberg, and F. Marquardt, Cavity optomechanics, Rev. Mod. Phys. **86**, 1391 (2014).

[9] X. Zhang, C.-L. Zou, L. Jiang, and H. Tang, Cavity magnonmechanics, Sci. Adv. **2**, e1501286 (2016).

[10] O. O. Soykal and M. E. Flatté, Strong Field Interactions between a Nanomagnet and a Photonic Cavity, Phys. Rev. Lett. **104**, 077202 (2010).

[11] O. O. Soykal and M. E. Flatté, Size dependence of strong coupling between nanomagnets and photonic cavities, Phys. Rev. B **82**, 104413 (2010).

[12] Z.-X. Liu, H. Xiong, and Y. Wu, Magnon blockade in a hybrid ferromagnet-superconductor quantum system, Phys. Rev. B **100**, 134421 (2019).

[13] J. Li, Y.-P. Wang, W.-J. Wu, S.-Y. Zhu, and J. You, Quantum network with magnonic and mechanical nodes, PRX Quantum **2**, 040344 (2021).

[14] Y. Tabuchi, S. Ishino, T. Ishikawa, R. Yamazaki, K. Usami, and Y. Nakamura, Hybridizing Ferromagnetic Magnons and Microwave Photons in the Quantum Limit, Phys. Rev. Lett. **113**, 083603 (2014).

[15] X. Zhang, C.-L. Zou, L. Jiang, and H. X. Tang, Strongly Coupled Magnons and Cavity Microwave Photons, Phys. Rev. Lett. **113**, 156401 (2014).

[16] M. Harder, P. Hyde, L. Bai, C. Match, and C.-M. Hu, Spin dynamical phase and antiresonance in a strongly coupled magnon-photon system, Phys. Rev. B **94**, 054403 (2016).

[17] P. Hyde, L. Bai, M. Harder, C. Dyck, and C.-M. Hu, Linking magnon-cavity strong coupling to magnon-polaritons through effective permeability, Phys. Rev. B **95**, 094416 (2017).

[18] Y.-P. Wang, G.-Q. Zhang, D. Zhang, T.-F. Li, C.-M. Hu, and J. Q. You, Bistability of Cavity Magnon Polaritons, Phys. Rev. Lett. **120**, 057202 (2018).

[19] R.-C. Shen, Y.-P. Wang, J. Li, S.-Y. Zhu, G. S. Agarwal, and J. Q. You, Long-Time Memory and Ternary Logic Gate Using a Multistable Cavity Magnonic System, Phys. Rev. Lett. **127**, 183202 (2021).

[20] Y. Tabuchi, S. Ishino, A. Noguchi, T. Ishikawa, R. Yamazaki, K. Usami, and Y. Nakamura, Coherent coupling between a ferromagnetic magnon and a superconducting qubit, Science **349**, 405 (2015).

[21] D. Lachance-Quirion, S. Piotr Wolski, Y. Tabuchi, S. Kono, K. Usami, and Y. Nakamura, Entanglement-based single-shot detection of a single magnon with a superconducting qubit, Science **367**, 425 (2020).

[22] J. Li, S.-Y. Zhu, and G. S. Agarwal, Magnon-Photon-Phonon Entanglement in Cavity Magnomechanics, Phys. Rev. Lett. **121**, 203601 (2018).

[23] J. Li and S.-Y. Zhu, Entangling two magnon modes via magnetostrictive interaction, New J. Phys. **21**, 085001 (2019).

[24] M. Yu, H. Shen, and J. Li, Magnetostrictively Induced Stationary Entanglement between Two Microwave Fields, Phys. Rev. Lett. **124**, 213604 (2020).

[25] Y.-T. Chen, L. Du, Y. Zhang, and J.-H. Wu, Perfect transfer of enhanced entanglement and asymmetric steering in a cavity-magnomechanical system, Phys. Rev. A **103**, 053712 (2021).

[26] S.-f. Qi and J. Jing, Magnon-assisted photon-phonon conversion in the presence of structured environments, Phys. Rev. A **103**, 043704 (2021).

[27] B. Sarma, T. Busch, and J. Twamley, Cavity magnomechanical storage and retrieval of quantum states, New J. Phys. **23**, 043041 (2021).

[28] S. Vashahri-Ghamsari, Q. Lin, B. He, and M. Xiao, Magnomechanical phonon laser beyond the steady state, Phys. Rev. A **104**, 033511 (2021).

[29] C. Liu, Z. Dutton, C. H. Behroozi, and L. V. Hau, Observation of coherent optical information storage in an atomic medium using halted light pulses, Nature (London) **409**, 490 (2001).

[30] J. I. Cirac, P. Zoller, H. J. Kimble, and H. Mabuchi, Quantum State Transfer and Entanglement Distribution among Distant Nodes in a Quantum Network, Phys. Rev. Lett. **78**, 3221 (1997).

[31] H. J. Kimble, The quantum internet, Nature (London) **453**, 1023 (2008).

[32] V. Fiore, Y. Yang, M. C. Kuzyk, R. Barbour, L. Tian, and H. Wang, Storing Optical Information as a Mechanical Excitation in a Silica Optomechanical Resonator, Phys. Rev. Lett. **107**, 133601 (2011).

[33] C. Genes, A. Mari, P. Tombesi, and D. Vitali, Robust entanglement of a micromechanical resonator with output optical fields, Phys. Rev. A **78**, 032316 (2008).

[34] P. Kumar and M. Bhattacharya, Single-photon transfer using levitated cavityless optomechanics, Phys. Rev. A **99**, 023811 (2019).

[35] C.-P. Ho and S.-Y. Tseng, Optimization of adiabaticity in coupled-waveguide devices using shortcuts to adiabaticity, Opt. Lett. **40**, 4831 (2015).

[36] D. Guéry-Odelin, A. Ruschhaupt, A. Kiely, E. Torrontegui, S. Martínez-Garaot, and J. G. Muga, Shortcuts to adiabaticity: Concepts, methods, and applications, Rev. Mod. Phys. **91**, 045001 (2019).

[37] E. Torrontegui, S. Ibáñez, S. Martínez-Garaot, M. Modugno, A. del Campo, D. Guéry-Odelin, A. Ruschhaupt, X. Chen, and J. G. Muga, Shortcuts to adiabaticity, Adv. At. Mol. Opt. Phys. **62**, 117 (2013).

[38] M. V. Berry, Transitionless quantum driving, J. Phys. A **42**, 365303 (2009).

[39] M. Demirplak and S. A. Rice, Assisted adiabatic passage revisited, J. Phys. Chem. B **109**, 6838 (2005).

[40] A. del Campo, Shortcuts to Adiabaticity by Counterdiabatic Driving, Phys. Rev. Lett. **111**, 100502 (2013).

[41] H. R. Lewis and W. B. Riesenfeld, An exact quantum theory of the time-dependent harmonic oscillator and of a charged particle in a time-dependent electromagnetic field, J. Math. Phys. **10**, 1458 (1969).

[42] B. d. L. Bernardo, Time-rescaled quantum dynamics as a shortcut to adiabaticity, Phys. Rev. Research **2**, 013133 (2020).

[43] B.-X. Wang, T. Xin, X.-Y. Kong, S.-J. Wei, D. Ruan, and G.-L. Long, Experimental realization of noise-induced adiabaticity in nuclear magnetic resonance, Phys. Rev. A **97**, 042345 (2018).

[44] J. Jing and L.-A. Wu, Overview of quantum memory protection and adiabaticity induction by fast signal control, Sci. Bull. **60**, 328 (2015).

[45] J. Jing, L.-A. Wu, T. Yu, J. Q. You, Z.-M. Wang, and L. Garcia, One-component dynamical equation and noise-induced adiabaticity, Phys. Rev. A **89**, 032110 (2014).

[46] X. Chen, I. Lizuain, A. Ruschhaupt, D. Guéry-Odelin, and J. G. Muga, Shortcut to Adiabatic Passage in Two- and Three-Level Atoms, Phys. Rev. Lett. **105**, 123003 (2010).

[47] S. Wu, W. Ma, X. Huang, and X. Yi, Shortcuts to Adiabaticity for Open Quantum Systems and a Mixed-State Inverse Engineering Scheme, Phys. Rev. Applied **16**, 044028 (2021).

[48] A. Vepsäläinen, S. Danilin, and G. S. Paraoanu, Superadiabatic population transfer in a three-level superconducting circuit, Sci. Adv. **5**, eaau5999 (2019).

[49] A. Tobalina, E. Torrontegui, I. Lizuain, M. Palmero, and J. G. Muga, Invariant-based inverse engineering of time-dependent, coupled harmonic oscillators, Phys. Rev. A **102**, 063112 (2020).

[50] Y.-H. Chen, Z.-C. Shi, J. Song, and Y. Xia, Invariant-based inverse engineering for fluctuation transfer between membranes in an optomechanical cavity system, Phys. Rev. A **97**, 023841 (2018).

[51] H. Zhang, X.-K. Song, Q. Ai, H. Wang, G.-J. Yang, and F.-G. Deng, Fast and robust quantum control for multimode interactions using shortcuts to adiabaticity, Opt. Express **27**, 7384 (2019).

[52] F.-Y. Zhang, W.-L. Li, W.-B. Yan, and Y. Xia, Speeding up adiabatic state conversion in optomechanical systems, J. Phys. B **52**, 115501 (2019).

[53] Y. Wang, J.-L. Wu, Y.-K. Feng, J.-X. Han, Y. Xia, Y.-Y. Jiang, and J. Song, Optimal control for robust photon state transfer in optomechanical systems, Ann. Phys. (Berlin, Ger.) **533**, 2000608 (2021).

[54] A. Ruschhaupt, X. Chen, D. Alonso, and J. G. Muga, Optimally robust shortcuts to population inversion in two-level quantum systems, New J. Phys. **14**, 093040 (2012).

[55] X.-K. Song, F. Meng, B.-J. Liu, D. Wang, L. Ye, and M.-H. Yung, Robust stimulated Raman shortcut-to-adiabatic passage with invariant-based optimal control, Opt. Express **29**, 7998 (2021).

[56] X.-T. Yu, Q. Zhang, Y. Ban, and X. Chen, Fast and robust control of two interacting spins, Phys. Rev. A **97**, 062317 (2018).

[57] Y. Tikochinsky, Transformation brackets for generalized Bogolyubov-boson transformations, J. Math. Phys. **19**, 270 (1978).